

Melting tungsten nanoparticles: a molecular dynamics study

Amitava Moitra^{1,2}, Sungho Kim^{1,2}, J. Houze^{1,2}, B. Jelinek^{1,2}, Seong-Jin Park², Randall M. German^{3,2}, M. F. Horstemeyer², and Seong-Gon Kim^{3,2}

¹ Department of Physics and Astronomy, Mississippi State University, Mississippi State, MS 39762, USA

² Center for Advanced Vehicular Systems, Mississippi State University, Mississippi State, MS 39762, USA

³ Department of Mechanical Engineering, Mississippi State University, Mississippi State, MS 39762, USA

Received: date / Revised version: date

Abstract. We report a molecular dynamics simulation of melting of tungsten (W) nanoparticles. The modified embedded atom method (MEAM) interatomic potentials are used to describe the interaction between tungsten atoms. The melting temperature of unsupported tungsten nanoparticles of different sizes are found to decrease as the size of the particles decreases. The melting temperature obtained in the present study is approximately a decreasing function of inverse radius, in a good agreement with the predictions of thermodynamic models. We also observed that the melting of a W nanoparticle is preceded by the premelting of its outer skin at a temperature lower than its melting temperature.

PACS. 61.46.Df Nanoparticles – 61.46.-w Nanoscale materials – 64.70.Dv Solid-liquid transitions – 65.80.+n Thermal properties of small particles, nanocrystals, and nanotubes

1 Introduction

Tungsten, along with its alloys and compounds, occupies a unique position in materials science. The material properties that make tungsten attractive to the metals industry are high density, hardness, melting temperature, elastic modulus, and conductivity in conjunction with the low thermal expansion. The combination of these unique properties explains the diverse applications of tungsten ranging from home lighting to thermonuclear fusion first-wall protection [1, 2]. With nanoscale tungsten powders available at a reasonable cost, its usage will increase greatly and a new approach is required to balance the size dependent advantages against the temperature dependent limitations. Therefore, it is of great importance to understand the thermal stability of tungsten nanoparticles for their applications at higher temperatures. It has been seen previously that nanoparticles exhibit significant decrease in melting temperatures compared to infinite bulk solids [3]. This is related to the fact that the liquid-vapor interface energy is generally lower than the average solid-vapor interface energy [4]. Based on thermodynamics, a phenomenological relation between the melting temperature and particle size has been obtained: the melting temperature of a nanoparticle decreases as inversely proportional to the particle diameter [3–5]. It is also known that premelting, the phenomenon where the surface atoms of nanoparticles lose their solid ordering and hence melt prior to complete melting of the whole particle [5–10], plays an

important role in understanding the melting of nanoparticles. On the other hand, the Hall-Petch effect—the hardness increases in proportional to the inverse square-root of grain size [11, 12]—suggests that significant opportunities exist if nanoscale powders could be consolidated to full densities with minimized coarsening. Hence, knowledge of accurate melting temperature for different particle size plays an important role for the advancement of present engineering and technological growth.

Molecular dynamics simulations offer an effective tool to study the melting and coalescence of nanoparticles [13, 14]. These atomistic simulations require accurate atomic interaction potentials to compute the total energy of the system. First-principles calculations can provide the most reliable interatomic potentials. However, realistic simulations of the melting of nanoparticles often require a number of atoms that renders these methods impractical: they either require too much computer memory or take too long to be completed in a reasonable amount of time. One alternative is to use empirical or semi-empirical interaction potentials that can be evaluated efficiently. In this study, we use the modified embedded atom method (MEAM) originally proposed by Baskes et al. [15, 16]. MEAM was the first semi-empirical atomic potential using a single formalism for fcc, bcc, hcp, diamond-structured materials and even gaseous elements, in good agreement with experiments or first-principles calculations [16, 17]. The MEAM is an extension of the embedded-atom method (EAM) [18–20] to include angular forces. Cherne et al. made a careful comparison of MEAM and EAM calculations in a liquid nickel system [21].

Atomistic simulations of a wide range of elements and alloys have been performed using the MEAM potentials. A realistic shear behavior for silicon was first obtained using the MEAM by Baskes et al. [15]. The MEAM was also applied to various single elements [16] and to silicon-nickel alloys and interfaces [22]. Gall et al [23] used the MEAM to model the tensile debonding of an aluminum-silicon interface. Lee and Baskes [24] extended the MEAM to include the second nearest-neighbor interactions. A new analytic modified embedded-atom method (AMEAM) many-body potential was also proposed and applied to several hcp metals, including Mg [25, 26]. For the Mg-Al alloy system, a set of EAM potentials has been developed using the “force matching” method by Liu et al [27]. Recently, a new set of MEAM potentials for Mg-Al alloy system was developed by Jelinek et al [28]. These new potentials show a significant improvement over the previously published potentials, especially for the surface formation, stacking faults, and point defect formation energies.

The paper is organized in the following manner. In Sec. 2, we give a brief review of the MEAM. In Sec. 3, the procedure for melting simulation is presented. MD simulation results are presented and discussed in Sec. 4. Finally, in Sec. 5, we summarize our findings.

2 MEAM theory

The total energy E of a system of atoms in the MEAM [29] is approximated as the sum of the atomic energies

$$E = \sum_i E_i. \quad (1)$$

The energy of atom i consists of the embedding energy and the pair potential terms:

$$E_i = F_i(\bar{\rho}_i) + \frac{1}{2} \sum_{j \neq i} \phi_{ij}(r_{ij}). \quad (2)$$

F_i is the embedding function of atom i , $\bar{\rho}_i$ is the background electron density at the site of atom i , and $\phi_{ij}(r_{ij})$ is the pair potential between atoms i and j separated by a distance r_{ij} . The embedding energy $F_i(\bar{\rho}_i)$ represents the energy cost to insert atom i at a site where the background electron density is $\bar{\rho}_i$. The embedding energy is given in the form

$$F_i(\bar{\rho}_i) = A_i E_i^0 \bar{\rho}_i \ln(\bar{\rho}_i), \quad (3)$$

where the sublimation energy E_i^0 and parameter A_i depend on the element type of atom i . The background electron density $\bar{\rho}_i$ is given by

$$\bar{\rho}_i = \frac{\rho_i^{(0)}}{\rho_i^0} G(\Gamma_i), \quad (4)$$

where

$$\Gamma_i = \sum_{k=1}^3 \bar{t}_i^{(k)} \left(\frac{\rho_i^{(k)}}{\rho_i^{(0)}} \right)^2 \quad (5)$$

and

$$G(\Gamma) = \sqrt{1 + \Gamma}. \quad (6)$$

The zeroth and higher order densities, $\rho_i^{(0)}$, $\rho_i^{(1)}$, $\rho_i^{(2)}$, and $\rho_i^{(3)}$ are given in Eq. (9). The composition-dependent electron density scaling ρ_i^0 is given by

$$\rho_i^0 = \rho_{i0} Z_{i0} G(\Gamma_i^{\text{ref}}), \quad (7)$$

where ρ_{i0} is an element-dependent density scaling, Z_{i0} is the first nearest-neighbor coordination of the reference system, and Γ_i^{ref} is given by

$$\Gamma_i^{\text{ref}} = \frac{1}{Z_{i0}^2} \sum_{k=1}^3 \bar{t}_i^{(k)} s_i^{(k)}, \quad (8)$$

where $s_i^{(k)}$ is the shape factor that depends on the reference structure for atom i . Shape factors for various structures are specified in the work of Baskes [16]. The partial electron densities are given by

$$\rho_i^{(0)} = \sum_{j \neq i} \rho_j^{a(0)} S_{ij} \quad (9a)$$

$$\left(\rho_i^{(1)} \right)^2 = \sum_{\alpha} \left[\sum_{j \neq i} \rho_j^{a(1)} \frac{r_{ij\alpha}}{r_{ij}} S_{ij} \right]^2 \quad (9b)$$

$$\left(\rho_i^{(2)} \right)^2 = \sum_{\alpha, \beta} \left[\sum_{j \neq i} \rho_j^{a(2)} \frac{r_{ij\alpha} r_{ij\beta}}{r_{ij}^2} S_{ij} \right]^2 - \frac{1}{3} \left[\sum_{j \neq i} \rho_j^{a(2)} S_{ij} \right]^2 \quad (9c)$$

$$\left(\rho_i^{(3)} \right)^2 = \sum_{\alpha, \beta, \gamma} \left[\sum_{j \neq i} \rho_j^{a(3)} \frac{r_{ij\alpha} r_{ij\beta} r_{ij\gamma}}{r_{ij}^3} S_{ij} \right]^2 - \frac{3}{5} \sum_{\alpha} \left[\sum_{j \neq i} \rho_j^{a(3)} \frac{r_{ij\alpha}}{r_{ij}} S_{ij} \right]^2, \quad (9d)$$

where $r_{ij\alpha}$ is the α component of the displacement vector from atom i to atom j . S_{ij} is the screening function between atoms i and j and is defined in Eqs. (16). The atomic electron densities are computed as

$$\rho_i^{a(k)}(r_{ij}) = \rho_{i0} \exp \left[-\beta_i^{(k)} \left(\frac{r_{ij}}{r_i^0} - 1 \right) \right], \quad (10)$$

where r_i^0 is the nearest-neighbor distance in the single-element reference structure and $\beta_i^{(k)}$ is element-dependent parameter. Finally, the average weighting factors are given by

$$\bar{t}_i^{(k)} = \frac{1}{\rho_i^{(0)}} \sum_{j \neq i} t_j^{(k)} \rho_j^{a(0)} S_{ij}, \quad (11)$$

where $t_j^{(k)}$ is an element-dependent parameter.

The pair potential is given by

$$\phi_{ij}(r_{ij}) = \bar{\phi}_{ij}(r_{ij})S_{ij} \quad (12)$$

$$\bar{\phi}_{ij}(r_{ij}) = \frac{1}{Z_{ij}} \left[2E_{ij}^u(r_{ij}) - F_i \left(\frac{Z_{ij}\rho_j^{(0)}(r_{ij})}{Z_i\rho_i^0} \right) - F_j \left(\frac{Z_{ij}\rho_i^{(0)}(r_{ij})}{Z_j\rho_j^0} \right) \right] \quad (13)$$

$$E_{ij}^u(r_{ij}) = -E_{ij}^0 (1 + a_{ij}^*(r_{ij})) e^{-a_{ij}^*(r_{ij})} \quad (14)$$

$$a_{ij}^* = \alpha_{ij} \left(\frac{r_{ij}}{r_{ij}^0} - 1 \right), \quad (15)$$

where α_{ij} is an element-dependent parameter. The sublimation energy E_{ij}^0 , the equilibrium nearest-neighbor distance r_{ij}^0 , and the number of nearest-neighbors Z_{ij} are obtained from the reference structure.

The screening function S_{ij} is designed so that $S_{ij} = 1$ if atoms i and j are unscreened and within the cutoff radius r_c , and $S_{ij} = 0$ if they are completely screened or outside the cutoff radius. It varies smoothly between 0 and 1 for partial screening. The total screening function is the product of a radial cutoff function and three-body terms involving all other atoms in the system:

$$S_{ij} = \bar{S}_{ij} f_c \left(\frac{r_c - r_{ij}}{\Delta r} \right) \quad (16a)$$

$$\bar{S}_{ij} = \prod_{k \neq i, j} S_{ikj} \quad (16b)$$

$$S_{ikj} = f_c \left(\frac{C_{ikj} - C_{\min, ikj}}{C_{\max, ikj} - C_{\min, ikj}} \right) \quad (16c)$$

$$C_{ikj} = 1 + 2 \frac{r_{ij}^2 r_{ik}^2 + r_{ij}^2 r_{jk}^2 - r_{ij}^4}{r_{ij}^4 - (r_{ik}^2 - r_{jk}^2)^2} \quad (16d)$$

$$f_c(x) = \begin{cases} 1 & x \geq 1 \\ [1 - (1 - x)^4]^2 & 0 < x < 1 \\ 0 & x \leq 0 \end{cases} \quad (16e)$$

Note that C_{\min} and C_{\max} can be defined separately for each i - j - k triplet, based on their element types. The parameter Δr controls the distance over which the radial cutoff function changes from 1 to 0 near $r = r_c$.

3 Molecular dynamics simulation

3.1 Atomic potential

We use the MEAM potential parameters for tungsten (W) proposed by Baskes [16]. The potential parameters that are used for our simulation of W nanoparticles are listed in Table 1. These parameters are obtained by fitting the room temperature elastic properties using bcc as the reference structure. C_{\max} and C_{\min} are chosen to consider only the first nearest-neighbor interactions [30].

We validate the potential by computing different physical properties of tungsten systems and comparing them with DFT calculations. The results are compared with those of DFT calculations as shown in Table 2. Energy calculations and geometry optimizations of various structures were performed using Blöchl's all-electron projector augmented wave (PAW) method [31] as implemented by Kresse and Joubert [32]. For the treatment of electron exchange and correlation, we use the generalized gradient approximation (GGA) using Perdew-Burke-Ernzerhof scheme [33].

3.2 Simulation Procedure

We performed a detailed MD simulation of the melting of unsupported spherical bcc W nanoparticles, 2–12 nm in diameter (259–56905 atoms). The surface boundary condition was free and no external pressure was applied. Each nanoparticle was constructed by cutting out atoms within a specified radius from the tungsten bulk in bcc structure. The equations of motion were integrated using time steps $\Delta t = 4 \times 10^{-15}$ s. We begin each MD run by randomizing the atomic velocities of the nanoparticle according to the Maxwell-Boltzmann distribution. We increase the temperature of the heat bath in steps of $\Delta T = 100$ K from the initial temperature $T_i = 500$ K to the final temperature up to $T_f = 4000$ K. We let the nanoparticles come to equilibration for 50 000 time steps at each temperature. Statistical (time-averaged) data for the energetics are collected after the system has adjusted to the new temperature, which is typically after 25 000 time steps following a temperature increase. For the particles of diameters less than 8 nm, 20 000 time steps were used to adjust the particles to each new temperature. The isothermal condition was maintained by using Nosé-Hoover thermostat [34, 35].

4 Results and Discussion

The most straightforward method to identify the melting of atomistic structures in MD simulations is to monitor the variation of the internal energy with temperature. Fig. 1 shows the internal energies of the W nanoparticles with different diameters as a function of temperature. It is clearly seen from the Fig. 1 that each internal energy curve goes from one linear region to another. The overall melting is clearly identified by the abrupt ‘‘jump’’ in the internal energy curve. The height of the jump is a measure of ΔH_m , the amount of heat required for melting, and it decreases as the size of nanoparticle decreases. The melting temperatures calculated based on the present MD simulation of W nanoparticles are listed in Table 3. We note that the melting temperature of bulk W from our MD simulation, 3900 K, is slightly higher than the experimentally measured value of 3695 K [36]. The discrepancy in this result is mainly due to the super-heating of the simulated lattice, as it has been observed that the confined lattice without free surface can be significantly superheated [37, 38]. Although, it is not the main focus

of this study, one can follow the procedure prescribed by Morris et al [39] to establish co-existence of solid and liquid phases to determine the melting temperature of the bulk W system without super-heating. More importantly, we also note that the melting temperature decreases drastically as the size of the particle decreases. This result suggests that the thermal stability of small nanoparticles must be carefully investigated before they can be used in applications such as nano-devices.

The melting behavior of 2 nm particle seems to be different from those of bigger particles: at the onset of the melting, the internal energy curve dips down before climbing up again. A similar behavior has been observed in the melting of small Au nanoparticles of diameters up to 2.8 nm [13]. The onset of melting provides surface atoms an opportunity to rearrange themselves to optimize the local morphology and lower their portion of the internal energy. For extremely small particles, where the surface area to volume ratio is large, this will cause the total internal energy of the particle to decrease briefly as shown in Fig. 1. However, a further detailed study focusing on small nanoparticles will be required to elucidate this peculiar behavior.

The variation of the melting temperature with the size of the W nanoparticles is plotted in Fig. 2. The melting point depression of W nanoparticles exhibit the same qualitative behavior found in the MD simulation of Au nanoparticles [9, 13]. A similar size dependence of melting point depression has been observed experimentally over a broad range of particle sizes for particles in cluster beams [40–43] as well as particles on substrates [6,7,44,45].

For spherical particles of diameter R , a melting temperature $T_m(R)$ can be obtained phenomenologically [4, 5, 46] by equating the Gibbs free energies of solid and liquid spherical clusters, assuming constant pressure conditions:

$$T_m(R) = T_m^* \left(1 - \frac{R_1}{R} \right), \quad (17)$$

where T_m^* is the melting temperature of the bulk tungsten and R_1 is a parameter related to physical quantities such as the solid and liquid densities, the bulk latent heat of melting, and solid-vapor and liquid-vapor interface energies. In obtaining this model, the surface energy anisotropy of the solid is not taken into account, and the possibility of inhomogeneous phases (such as a liquid layer due to premelting) is also neglected. The solid line in Fig. 2 corresponds to the simple thermodynamical model of Eq. (17), with constant parameters $T^* = 2900$ K and $R_1 = 1.5$ nm. The curve shows clearly that the melting point of W nanoparticles decrease according to $1/R$ dependence as predicted in Eq. (17). However, the fitted value of T^* is significantly lower than the melting temperature of the bulk tungsten. This result indicates that the characteristics of the curve is likely to change for nanoparticles with larger diameters, and further study with larger nanoparticles will be needed to test the applicability of this model to W nanoparticles.

Hansen [47] proposed another model of melting in terms of classical thermodynamics assuming that a liq-

uid over-layer forms at the surface of the solid cluster and grows towards the solid core, below the melting point [48, 49]. When the liquid layer thickness exceeds a critical thickness, the whole cluster melts homogeneously. In this model, the melting point $T_m(R)$ of W nanoparticles with diameter R can be expressed as [6, 7]

$$T_m(R) = T_m^* \left(1 - \frac{R_1}{R - t_0} + \frac{R_2}{R} \right), \quad (18)$$

When the data of Table 3 were fitted to Eq. (18), we obtained negligibly small values for t_0 and R_2 , thus returning to the model of Eq. (17).

Fig. 3 shows the cross sections of a W nanoparticle with a diameter 10 nm through the center of the particle. The displacement vectors at different times during the MD simulation run at the temperature 2000 K are plotted. Fig. 3 shows that at a temperature below the melting point the atoms in the entire nanoparticle vibrate in their places while retaining their bcc crystal structure. As the temperature increase, several layers of atoms start to lose their periodicity and form a liquid shell as shown in Fig. 3(b). Once the thickness of the liquid layer reaches a critical thickness, the whole nanoparticle melts. Our MD simulation confirms the experimental observation that nanoscale materials simultaneously display solid-like and liquid-like characteristics, and under thermodynamic equilibrium, a fraction of the atoms in the outer shell of the particle exhibit liquid-like behavior and the remaining fraction in the inner core act as solid [7]. Hence, melting point depression and the presence of disorder in nanoscale W powders will play an important role in various industries, including microelectronic industries such as printed circuit board drill bits [50].

Fig. 4 shows a few snapshots of MD simulation for a small W nanoparticle with the diameter of 2 nm. We note that our simulations does not show pronounced faceted or step-like structures. We found a similar result when the nanoparticles are heated to the melting temperature and cooled down slowly. Our results are in good agreement with an earlier experiment that found no evidence for a faceted or step-like microstructure in a single tungsten crystal [51].

5 Conclusions

The thermal stability of unsupported W nanoparticles has been investigated using a MD simulation. The MEAM potential was used to described the interatomic interactions. W nanoparticles melt at a temperature that is lower than the bulk melting temperature. The result of our present calculation shows that the melting temperature to be approximately a decreasing function of inverse radius. We found that W nanoparticle melting is preceded by surface melting effects of its outer skin, similar to the melting of spherical clusters of many other elements.

6 Acknowledgment

The authors are grateful to the Center for Advanced Vehicular Systems at Mississippi State University for supporting this study. Computer time allocation has been provided by the High Performance Computing Collaboratory (HPC²) at Mississippi State University.

References

1. S. W. H. Yih and C. T. Wang. *Tungsten: Sources, Metallurgy, Properties, and Applications*. Plenum Press, New York, 1979.
2. E. Lassner and W. D. Schubert. *Tungsten: Properties, Chemistry, Technology of the Element*. Kluwer Academic / Plenum Publishers, 1999.
3. J. P. Borel. Thermodynamical size effect and the structure of metallic clusters. *Surf. Sci.*, 106:1, 1981.
4. O. Gülseren, F. Ercolessi, and E. Tosatti. Premelting of thin wires. *Phys. Rev. B*, 51(11):7377–7380, Mar 1995.
5. P. Pawlow. *Z. Phys. Chem.*, 65:545, 1909.
6. S. L. Lai, J. Y. Guo, V. Petrova, G. Ramanath, and L. H. Allen. Size-dependent melting properties of small tin particles: Nanocalorimetric measurements. *Phys. Rev. Lett.*, 77(1):99, Jul 1996.
7. S. L. Lai, J. R. A. Carlsson, and L. H. Allen. Melting point depression of Al clusters generated during the early stages of film growth: Nanocalorimetry measurements. *Applied Physics Letters*, 72(9):1098–1100, 1998.
8. J. Frenken and J. Vanderveen. *Phys. Rev. Lett.*, 54:134, 1985.
9. Furio Ercolessi, Wanda Andreoni, and Erio Tosatti. Melting of small gold particles: Mechanism and size effects. *Phys. Rev. Lett.*, 66(7):911–914, Feb 1991.
10. Laurent J. Lewis, Pablo Jensen, and Jean-Louis Barrat. Melting, freezing, and coalescence of gold nanoclusters. *Phys. Rev. B*, 56(4):2248–2257, Jul 1997.
11. E. O. Hall. *Proc. Phys. Soc., Ser. B*, 64:747–753, 1951.
12. N. J. Petch. *J. Iron and Steel Institute*, pages 25–28, 1953.
13. Shim J.-H., Lee B.-J., and Cho Y.W. Thermal stability of unsupported gold nanoparticle: a molecular dynamics study. *Surface Science*, 512:262–268, 2002.
14. Seong-Gon Kim and David Tománek. Melting the fullerenes: A molecular dynamics study. *Phys. Rev. Lett.*, 72(15):2418–2421, Apr 1994.
15. M. I. Baskes, J. S. Nelson, and A. F. Wright. Semiempirical modified embedded-atom potentials for silicon and germanium. *Phys. Rev. B*, 40(9):6085–6100, Sep 1989.
16. M. I. Baskes. Modified embedded-atom potentials for cubic materials and impurities. *Phys. Rev. B*, 46(5):2727–2742, Aug 1992.
17. M. I. Baskes and R. A. Johnson. Modified embedded atom potentials for hcp metals. *Modell. Simul. Mater. Sci. Eng.*, 2(1):147–163, 1994.
18. Murray S. Daw. Model of metallic cohesion: The embedded-atom method. *Phys. Rev. B*, 39(11):7441–7452, Apr 1989.
19. Murray S. Daw and M. I. Baskes. Embedded-atom method: Derivation and application to impurities, surfaces, and other defects in metals. *Phys. Rev. B*, 29(12):6443–6453, Jun 1984.
20. Murray S. Daw and M. I. Baskes. Semiempirical, quantum mechanical calculation of hydrogen embrittlement in metals. *Phys. Rev. Lett.*, 50(17):1285–1288, Apr 1983.
21. F. J. Cherne, M. I. Baskes, and P. A. Deymier. Properties of liquid nickel: A critical comparison of eam and meam calculations. *Phys. Rev. B*, 65(2):024209, Dec 2001.
22. M. I. Baskes, J. E. Angelo, and C. L. Bisson. Atomistic calculations of composite interfaces. *Modell. Simul. Mater. Sci. Eng.*, 2(3A):505–518, 1994.
23. K. Gall, M.F. Horstemeyer, M. Van Schilfhaarde, and M.I. Baskes. Atomistic simulations on the tensile debonding of an aluminum-silicon interface. *J. Mech. Phys. Solids*, 48:2183–2212, 2000.
24. Byeong-Joo Lee and M. I. Baskes. Second nearest-neighbor modified embedded-atom-method potential. *Phys. Rev. B*, 62(13):8564–8567, Oct 2000.
25. Wangyu Hu, Bangwei Zhang, Baiyun Huang, Fei Gao, and David J Bacon. Analytic modified embedded atom potentials for hcp metals. *J. Phys.: Condens. Matter*, 13(6):1193–1213, 2001.
26. Wangyu Hu, Huiqiu Deng, Xiaojian Yuan, and Masahiro Fukumoto. Point-defect properties in hcp rare earth metals with analytic modified embedded atom potentials. *Eur. Phys. J. B*, 34(4):429–440, 2003.
27. X.-Y. Liu, P.P. Ohotnicky, J.B. Adams, C.L. Rohrer, and R.W.J. Hyland. Anisotropic surface segregation in Al-Mg alloys. *Surface Science*, 373:357–370, 1997.
28. B. Jelinek, J. Houze, Sungho Kim, M. F. Horstemeyer, M. I. Baskes, and Seong-Gon Kim. Modified embedded-atom method interatomic potentials for the Mg-Al alloy system. *Phys. Rev. B*, 75(5):054106, 2007.
29. Young-Min Kim, Byeong-Joo Lee, and M. I. Baskes. Modified embedded-atom method interatomic potentials for Ti and Zr. *Phys. Rev. B*, 74(1):014101, 2006.
30. M. I. Baskes. Determination of modified embedded atom method parameters for nickel. *Mater. Chem. Phys.*, 50, 1997.
31. P. E. Blöchl. Projector augmented-wave method. *Phys. Rev. B*, 50(24):17953–17979, Dec 1994.
32. G. Kresse and D. Joubert. From ultrasoft pseudopotentials to the projector augmented-wave method. *Phys. Rev. B*, 59(3):1758–1775, Jan 1999.
33. J. P. Perdew, K. Burke, and M. Ernzerhof. Generalized Gradient Approximation Made Simple. *Phys. Rev. Lett.*, 77:3865–3868, 1996.
34. William G. Hoover. Canonical dynamics: Equilibrium phase-space distributions. *Phys. Rev. A*, 31(3):1695–1697, Mar 1985.
35. Shuichi Nosé. A unified formulation of the constant temperature molecular dynamics methods. *J. Chem. Phys.*, 81(1):511–519, 1984.
36. John Emsley. *The Elements*. Oxford University Press, Oxford, UK, 3rd. edition, 1998.
37. Z. H. Jin and K. Lu. To what extent can a crystal be superheated? *Nanostruct. Mater.*, 12:369–372, 1999.
38. K. Lu and Y. Li. Homogeneous nucleation catastrophe as a kinetic stability limit for superheated crystal. *Phys. Rev. Lett.*, 80(20):4474–4477, May 1998.
39. J. R. Morris, C. Z. Wang, K. M. Ho, and C. T. Chan. Melting line of aluminum from simulations of coexisting phases. *Phys. Rev. B*, 49(5):3109–3115, Feb 1994.
40. George Bertsch. CONDENSED MATTER PHYSICS: Enhanced: Melting in Clusters. *Science*, 277(5332):1619–, 1997.

41. R. S. Berry. When the melting. and freezing points are not the same. *Scientific American*, 263:68, 1990.
42. Martin Schmidt, Robert Kusche, Bernd von Issendorff, and Hellmut Haberland. Irregular variations in the melting point of size-selected atomic clusters. *Nature*, 393:238–240, 1998.
43. Martin Schmidt, Robert Kusche, Werner Kronmüller, Bernd von Issendorff, and Hellmut Haberland. Experimental determination of the melting point and heat capacity for a free cluster of 139 sodium atoms. *Phys. Rev. Lett.*, 79(1):99, Jul 1997.
44. G L Allen, R A Bayles, W W Gile, and W A Jesser. Small particle melting of pure metals. *Thin Solid Films*, 144:297–308, 1986.
45. Kevin F. Peters, Jerome B. Cohen, and Yip-Wah Chung. Melting of pb nanocrystals. *Phys. Rev. B*, 57(21):13430–13438, Jun 1998.
46. Ph. Buffat and J-P. Borel. Size effect on the melting temperature of gold particles. *Phys. Rev. A*, 13(6):2287–2298, Jun 1976.
47. K.-J. Hanszen. *Z. Phys.*, 157:523–553, 1960.
48. M. Yu. Efremov, F. Schiettekatte, M. Zhang, E. A. Olson, A. T. Kwan, R. S. Berry, and L. H. Allen. Discrete periodic melting point observations for nanostructure ensembles. *Phys. Rev. Lett.*, 85(17):3560–3563, Oct 2000.
49. M. Zhang, M. Yu. Efremov, F. Schiettekatte, E. A. Olson, A. T. Kwan, S. L. Lai, T. Wisleder, J. E. Greene, and L. H. Allen. Size-dependent melting point depression of nanostructures: nanocalorimetric measurements. *Phys. Rev. B*, 62(15):10548–10557, Oct 2000.
50. G. B. Gille and G. Leitner. *International Journal of Refractory Metals and Hard Materials*, 20:3–22, 2002.
51. S. T. Martin. On the thermionic and adsorptive properties of the surfaces of a tungsten single crystal. *Phys. Rev.*, 56(9):947–959, Nov 1939.

Table 2. Calculated physical properties of W using the present MEAM parameters in comparison with DFT calculations. B_0 is the bulk modulus (GPa); C_{11} , C_{12} , C_{44} are the elastic constants (GPa); $E_{(100)}$, $E_{(110)}$, $E_{(111)}$ are surface energies of corresponding surfaces (mJ/m^2); ΔE 's are the structural energy differences (eV/atom).

Parameter	DFT	MEAM
B_0	330	270
$(C_{11} - C_{12})/2$	190	160
C_{44}	280	160
$E_{(100)}$	7810	5980
$E_{(110)}$	6390	5660
$E_{(111)}$	7190	5030
$\Delta E_{\text{bcc} \rightarrow \text{fcc}}$	0.494	0.325
$\Delta E_{\text{bcc} \rightarrow \text{hcp}}$	0.397	2.168

Table 3. Melting temperatures of W nanoparticles with different diameters

Diameter (nm)	No. of atoms	T_m (K)
2.0	259	1000
4.0	2085	1900
6.0	7119	2200
8.0	16865	2300
10.0	33079	2400
12.0	56905	2500
Bulk	∞	3900

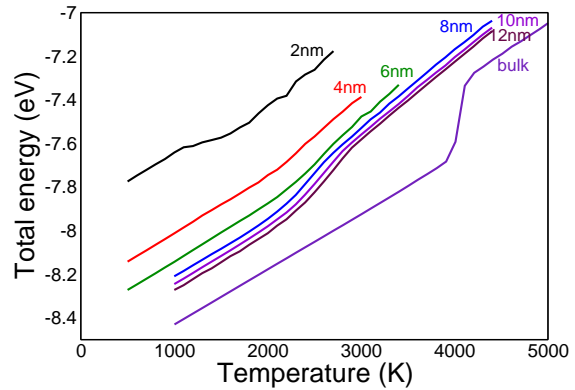


Fig. 1. Internal energies of the W nanoparticles with different diameters as a function of temperature. The same data for W bulk are also shown.

Table 1. The MEAM potential parameters for W from Ref. 30. E^0 is the sublimation energy, r^0 is the equilibrium nearest-neighbor distance, A is the scaling factor for the embedding energy, α is the exponential decay factor for the universal energy function, $\beta^{(0-3)}$ are the exponential decay factors for the atomic densities, $t^{(0-3)}$ are the weighting factors for the atomic densities, C_{\max} and C_{\min} are the screening parameters.

E^0 [eV]	r^0 [Å]	A	α	$\beta^{(0)}$	$\beta^{(1)}$	$\beta^{(2)}$	$\beta^{(3)}$	$t^{(0)}$	$t^{(1)}$	$t^{(2)}$	$t^{(3)}$	C_{\max}	C_{\min}
8.66	2.74	0.98	5.63	3.98	1.00	1.00	1.00	1.00	3.16	8.25	-2.70	2.8	2.0

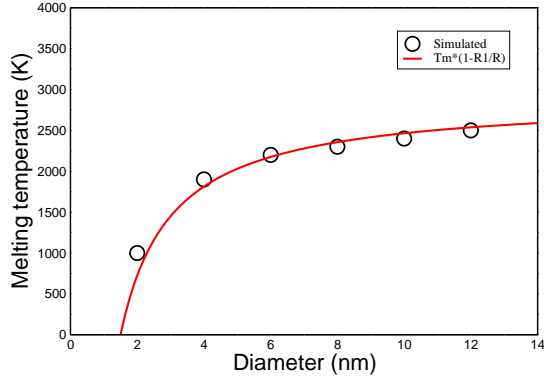


Fig. 2. Size dependence of the melting temperatures of W nanoparticles. Symbols represent the calculated values from the present MD simulation and the solid line is calculated in terms of Eq. (17).

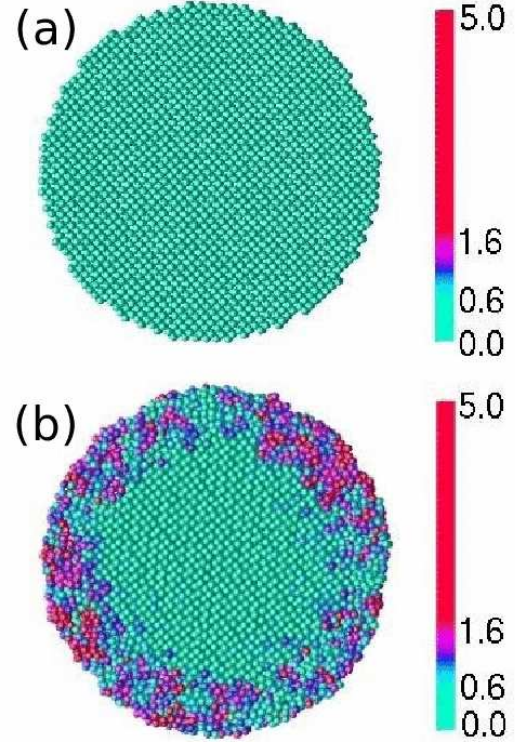


Fig. 3. (color online). The cross section of W nanoparticle with a diameter 10 nm through the center of the particle showing the displacement vectors in the interval of 6 ps at the temperature of (a) 300 K and (b) 2000 K. The color and the size of the spheres represent the magnitude of the displacement vectors.

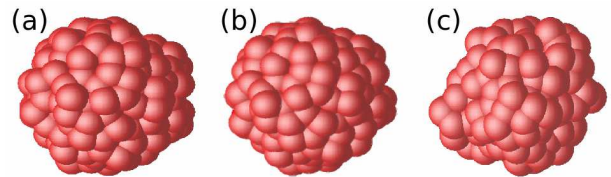


Fig. 4. Snapshots of MD simulation at (a) 300 K, (b) 900 K, and (c) 1500 K (above the melting temperature) for 2 nm particle.